IEEE Access
Multidisciplinary | Rapid Review | Open Access Journal

Received February 5, 2019, accepted February 26, 2019, date of publication March 12, 2019, date of current version April 2, 2019.

Digital Object Identifier 10.1109/ACCESS.2019.2904392

Computationally Efficient Distributed Predictive Controller for Cascaded Multilevel Impedance Source Inverter With LVRT Capability

MITCHELL EASLEY[1], (Student Member, IEEE), SARTHAK JAIN[2], (Member, IEEE), MOHAMMAD B. SHADMAND[1], (Member, IEEE), AND HAITHAM ABU-RUB[3], (Fellow, IEEE)

[1]Electrical and Computer Engineering Department, Kansas State University, Manhattan, KS 66506, USA
[2]Core Power Solutions Group, Renesas Electronics America, Milpitas, CA 95035, USA
[3]Department of Electrical and Computer Engineering, Texas A&M University at Qatar, Doha, Qatar

Corresponding author: Mohammad B. Shadmand (mshadmand@ksu.edu)

This publication was made possible by NPRP-EP grant # X-033-2-007 from the Qatar National Research Fund (a member of Qatar Foundation). The statements made herein are solely the responsibilities of the authors.

ABSTRACT This paper presents a decoupled active and reactive power control scheme for grid-tied quasi-impedance source cascaded multilevel inverter (qZS-CMI). For photovoltaic (PV) applications, the proposed control scheme is based on an enhanced finite-set model predictive control (MPC) to harvest the desired active power from the PV modules with the ability to provide the ancillary services for the grid. The proposed control scheme has two modes of operation: normal grid mode and low voltage ride through (LVRT) mode. In normal grid mode, the controller commands the qZS-CMI to operate at the global maximum power point (MPP). The proposed technique regulates the impedance network's current and voltage according to the MPP of PV strings and grid current/voltage requirements. In LVRT mode, the controller commands the qZS-CMI to provide the required reactive power to the grid during voltage sags as an ancillary service from the inverter as imposed by the grid codes. The main features of the proposed system include the global MPP operation during normal grid condition, LVRT capability during a grid voltage sag, mitigation of the PV modules mismatch effect on overall energy harvesting, seamless transition between a normal grid and LVRT modes of operation, and an efficient predictive controller that exploits the model redundancies in the control objectives. Several real-time experiments are conducted to verify the system performance with transients in both the solar irradiance and the grid voltage.

INDEX TERMS Impedance source inverter, LVRT, model predictive control, photovoltaic systems, reactive power compensator.

NOMENCLATURE

CMI	Cascaded Multilevel Inverter
CP	Cost Package
DG	Distributed Generation
LVRT	Low Voltage Ride Through
MPC	Model Predictive Control
MPP	Maximum Power Point
MPPT	Maximum Power Point Tracking
NST	Non-Shoot-Through
OSG	Orthogonal Signal Generator
PEI	Power Electronics Interface
PV	Photovoltaic
qZS	Quasi Z Source
qZSI	Quasi Z Source Inverter
RES	Renewable Energy Source
RMS	Root Mean Square
RPI	Reactive Power Injection
SOGI	Second-Order Generalized Integrator
ST	Shoot-Through
THD	Total Harmonic Distortion
VSI	Voltage Source Inverter
ZSI	Impedance (Z) Source Inverter

The associate editor coordinating the review of this manuscript and approving it for publication was Reinaldo Tonkoski.

I. INTRODUCTION

Voltage Source inverters (VSI) are widely used in photovoltaic (PV) grid-connected inverter applications. They can only be operated in buck mode and thus generally require multi-stage solution to interface low voltage PV strings. The

first stage performs DC/DC boost conversion and maximum power point tracking (MPPT) of PV, and the second stage performs DC/AC conversion using a VSI [1]–[6]. The use of cascaded multilevel inverter (CMI) topology is practical for PV energy harvesting systems, as the MPPT can be modularized for each VSI cell thus requiring less voltage across each VSI [7]. This would also able to address the mismatch in PV module voltage-current characteristics, caused by either manufacturing differences or inconsistencies in solar irradiance. In this paper, both issues will be generally referred to as PV mismatch. Additionally, the diminished harmonic content of the CMI output voltage can reduce output filter requirements to adhere to grid THD standards [8], [9]. However, the double stage configuration of the CMI cells decreases the overall system efficiency, incurs low transient response, etc [10]–[13]. Removing the DC/DC boost conversion stage and coupling the PVs to their DC bus would mitigate this, but will lead to unbalanced DC link voltage under PV mismatch scenarios [14] and diminish the MPP operating capability.

The voltage-fed Z-Source Inverter (ZSI) [15] has some benefits over the traditional VSI/CSI and can achieve both buck and boost operations and thus can directly couple the PV with the grid in a single-stage manner. The ZSI incorporates an impedance network between the DC source and the inverter bridge. This allows for an additional switching state, often called the shoot-through state, enabling buck/boost capabilities. The quasi Z-source inverter (qZSI) is an improvement over the ZSI, as it prevents discontinuous current at the PV side, increasing the lifespan of the PVs [16]. The qZSI can replace the traditional full-bridge inverter cells of the CMI, referred to as the quasi-Z-source cascaded multilevel inverter (qZS-CMI). However, incorporating an appropriate shoot-through duty ratio requires implementation of a complex switching modulator. Additionally, distributed generation (DG) should provide ancillary services to achieve a resilient utility grid, this feature requires a complex multiloop control scheme when using classical control approaches particularly for qZS-CMI [17], [18].

Finite-set model predictive control (MPC) is a potential candidate to address the challenges in the control of grid-tied qZS-CMI with advanced functionalities such as ancillary grid services. Finite-set MPC eliminates the need for a switching modulator. In addition, multi-objective control schemes can be implemented in a straightforward manner. However, traditional finite-set MPC optimizes its control objectives via an overall cost function, in which all predicted errors on control objectives are evaluated and summed for each achievable switching state. This requires tuning the weight factors of each control objective. There is no standard method for this procedure, and suggested procedures such as branch-and-bound [19] are particularly arduous for MPC schemes with more than two objectives. Traditional finite-set MPC is also computationally burdensome, especially for cascaded multilevel inverter topologies and other topologies with large sets of switching states, and thus may not achieve feasible sampling frequencies.

The analysis of qZS-CMI topologies is investigated in [20]–[23]. In [24], MPC for a grid-tied qZS multilevel inverter is proposed; however non-linearities and fluctuations of PV sources are not considered in the control scheme. Further, it does not investigate the ability to provide ancillary grid services, which will be necessary for a high PV-penetrated grid. The power electronics interface (PEI) for grid-tied renewable energy sources (RES) should be able to support the grid resiliency in addition to the extraction and transfer of power from RES to grid. E.ON-Netz grid code [25] mandates the low voltage ride through (LVRT) capability of PEI, which requires the PEI to retain grid connection and inject reactive power during grid voltage sag for a pre-defined amount of time. The E.ON suggests that PEI must inject entirely reactive power if grid voltage drops below 50% of the rated value [25].

Although MPC for the qZS-CMI topology has not been studied in literature to our knowledge, MPC techniques have been discussed for the CMI [26]–[28]. Cortés *et al.* [28] discuss MPC of a three-phase CMI with an RL load. The authors note the problem of increased calculations with multilevel topologies and mitigate this for their application by removing redundant voltage vectors with high common-mode voltage. Only current control is implemented for this MPC scheme, and redundant switching states are determined according to the output voltage vector. However, when MPC is used for both AC and DC-side control in a grid-connected application, this method of switching state elimination is not applicable.

This paper proposes a computationally efficient decoupled active and reactive power control scheme via MPC framework for a single phase qZS-CMI with 5-level output voltage. The decoupled power control scheme is advantageous to regulate the required reactive power and adjust active power injection independently during LVRT grid fault conditions. The novel control structure eliminates the overall cost function and applies a hierarchical objective structure that has been optimized offline to remove superfluous cost computations for practical realization of MPC for multilevel inverters. The remainder of this paper is organized as follows: Section II explains the grid-tied qZS-CMI as a primer to the control system. Section III describes the predictive model and reference signal generation, which are the inputs to the controller. In section IV, the novel and highly efficient predictive controller is explained. In section V, the controller performance is verified through several case studies. Finally, a summary of the findings are provided with the conclusion in Section VI.

II. PROPOSED SYSTEM DESCRIPTION

Fig. 1 shows the qZS-CMI along with its predictive decoupled active and reactive power control scheme. Five-level qZS-CMI is interfaced with single-phase 120VRMS, 60Hz grid. The controller works in two modes of operation: i) normal grid mode when grid voltage sag is not more than 10% of its rating, in this mode the MPPT technique is

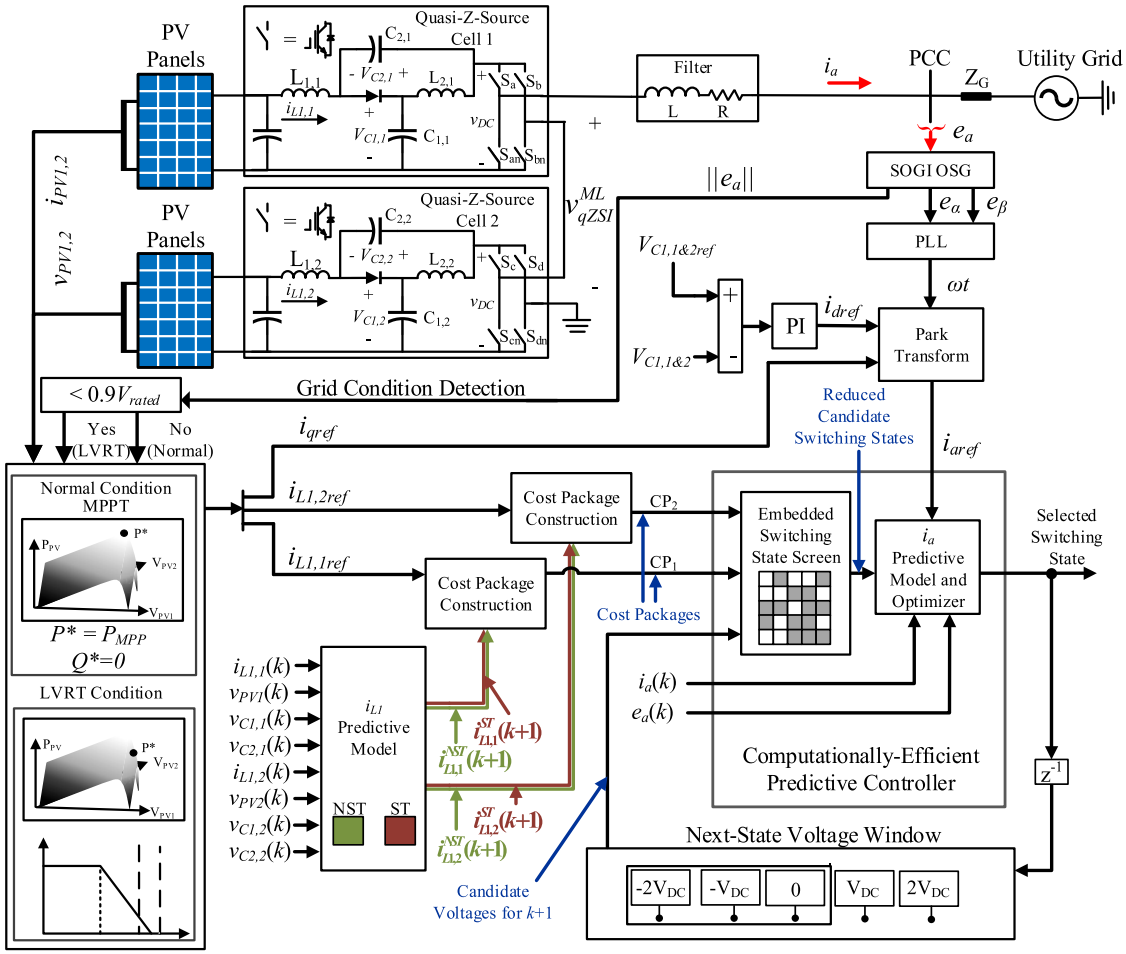

FIGURE 1. Proposed power electronics interface overview for PV applications with LVRT capability.

triggered to harvest the global maximum power from the PV cells; and ii) the LVRT mode for grid voltage sags of more than 10% threshold. In this mode, the qZS-CMI will move from MPP operation to support grid based on desired reactive power injection (RPI) strategies [29].

A. NORMAL GIRD MODE

A modified Perturb and Observe based MPPT with adaptive power generation constraint is used to generate the PV current reference or qZSI input inductor ($L_{1,1}$, $L_{1,2}$) current reference. Two independent PI controllers for both qZSI cells are used to generate the respective active current reference which upon summation gives the total i_d needed for injection to the grid by qZS-CMI. In this mode, reactive power component i_q is kept at zero, making the qZS-CMI inject purely active power to the grid. The final i_d and i_q then transformed into stationary frame to compose $i_{a,ref}$ along with the $i_{L1,1}$ and $i_{L1,2}$ references from MPPT algorithm. The MPPT algorithm contains an adaptive power point to facilitate the dual-mode operation of the proposed system; the MPPT algorithm is explained in more detail in section II.C.

B. LOW VOLTAGE RIDE THROUGH MODE

This mode is triggered when the grid voltage is less than 90% of its rated magnitude. A PLL with a second order generalized integrator (SOGI) based orthogonal signal generator (OSG) [30] is used to detect the grid voltage magnitude as well as its phase angle at PCC for the control scheme as illustrated in Fig. 1. The LVRT mode operation performance is tested for three reactive power injection strategies introduced in [29]: constant average active power, constant peak current, and constant active current.

In constant average active power strategy, the reactive power reference is added to the maximum real power harnessed from the PVs to determine the overall current to be injected into the grid. In constant peak current strategy, if the summation of active and reactive current components exceeds the peak current limit, real power from the PV is decreased to the right of the P-V curve. This maintains the peak current value within the pre-defined limit, thus providing inherent overcurrent protection during LVRT conditions. While, the constant active current strategy is the middle ground of the two other methods. The active current component is not increased to compensate for the voltage

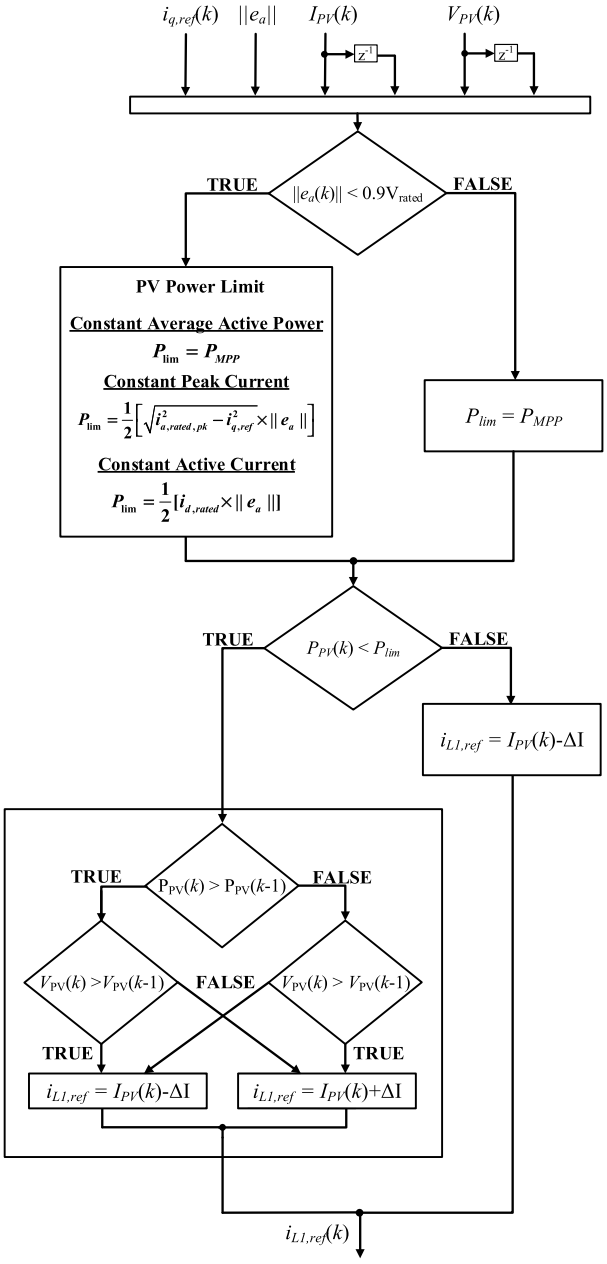

FIGURE 2. MPPT algorithm with adaptive power point.

sag, unlike in the constant average active power strategy. It will thus decrease active power injected to the grid. Overcurrent risks are apparent with this strategy but are less severe than the constant average active power strategy. These strategies will be explained in greater detail in the following section.

C. MPPT WITH ADAPTIVE POWER GENERATION

While this system operates with centralized controller that is common to all the systems' PV modules, each PV module holds its own MPPT algorithm, where it adjusts the power according to the grid condition. This allows each PV module to operate independently, making the system more robust to PV mismatching conditions. The algorithm in place of conventional MPPT is shown in Fig. 2. This allows the power point to be pulled away from the MPP, in accordance with the RPI strategy. The MPPT algorithm is adjusted to adhere to:

$$P_{PV} = \begin{cases} P_{MPP}, P_{PV} < \mathrm{P_{lim}} \\ P_{\mathrm{lim}}, P_{PV} \geq \mathrm{P_{lim}} \end{cases} \quad (1)$$

In MPPT mode, the P_{lim} is set to the maximum power that can be extracted from the PV strings (P_{MPP}), thus the algorithm works as a MPP tracker. In LVRT mode, the P_{lim} may be adjusted according to RPI strategy. When $\mathrm{P_{PV}(k)}$ exceeds $P_{lim}(\mathrm{k})$, the current reference decreases, increasing the operating voltage and pulling the operating point to the right of the MPP (according to the P-V characteristic curve). The operating point will continue to fall until $\mathrm{P_{PV}}(k)$ falls below $P_{lim}(k)$, where it will then settle at the new operating point. The $P_{lim}(k)$ calculation for each RPI strategy is explained below:

Constant average active power strategy: $P_{lim}(k)$ is kept constant at the maximum power point during voltage sags, thus the control will continue to extract constant power when transitioning in and out of LVRT mode.

Constant active current strategy: Unlike constant average active power strategy where the active current component will increase to compensate for the voltage sag, active power injection will adapt to the grid's condition for this RPI strategy. The new power reference is calculated as:

$$P_{\mathrm{lim}}(k) = \frac{1}{2}[i_{d,rated} \times e_{a,pk}(k)] \quad (2)$$

where $i_{d,rated}$ is the peak of the injected current in MPPT mode. The new peak of the grid voltage is detected:

$$e_{a,pk}(k) = \sqrt{e_d(k)^2 + e_q(k)^2} \quad (3)$$

where $e_d(k)$ and $e_q(k)$ are the decoupled grid voltage components in the rotating frame, determined from the stationary reference frame grid components by SOGI based OSG. The power transferred from the PV to the grid will ensure the active component of the current remains constant, but overall PV power extraction will decrease in proportion to the grid voltage sag.

Constant peak current strategy: This strategy considers the current limit of the inverter, by factoring in the reactive current to be injected according to grid codes. Here, the power reference is determined by:

$$P_{\mathrm{lim}}(k) = \frac{1}{2}\left[\sqrt{i_{a,rated,pk}^2 - i_{q,ref}^2} \times e_{a,pk}(k)\right] \quad (4)$$

where $i_{q,ref}$ is the peak reactive current that conforms to grid codes for the given voltage sag. Extracting this power from the PV string ensures the peak current will not exceed the inverter's rated current when the control transitions to LVRT mode.

TABLE 1. Dynamic equations of qZS cells.

State	v_{L1}	v_{L2}	v_{DC}	v_{diode}
Active/Null	$V_{PV}-V_{C1}$	$-V_{C2}$	$V_{C1}+V_{C2}$	0
Shoot through	$V_{PV}+V_{C2}$	V_{C1}	0	$-V_{C1}$-V_{C2}

III. PREDICTIVE MODEL AND REFERENCE GENERATION

A distributed predictive control strategy is proposed for the qZS-CMI; the i_{L1} control is modularized for each PV string, while the injected grid-side current is accumulated from each qZSI cell. In general, a finite-set model predictive controller has three components: the predictive model, reference signal generation, and cost function optimization. The proposed controller does not implement an overall cost function, thus the first two components are discussed in this section, and the optimization is discussed in the following section.

A. PREDICTIVE MODEL

Each qZSI cell is analyzed for both of its active and shoot-through states of operation which is required to develop predictive model equations for the control implementation. Table I shows the dynamic equations of qZSI in both active/non-shoot-through and shoot-through states. The grid current predictive model derives from the AC-side KVL equation:

$$v_{qZSI}^{ML} = Ri_a + L\frac{di_a}{dt} + e_a \tag{5}$$

where $v^{ML}{}_{qZSI}$ denotes the voltage vector which is the summation of the voltage vectors by both qZSI cells as shown in Fig. 1. i_a is the injected current to the grid, L is the filter inductance with R as its equivalent series resistance. Discretizing the differential term in (5) with the forward Euler approximation and rearranging terms gives the next-state prediction of i_a:

$$i_a(k+1) = i_a(k)\left[1 - \frac{R}{L}T_S\right] + \frac{T_S}{L}(v_{qZSI}^{ML}(k) - e_a(k)) \tag{6}$$

The predicted inductor current i_{L1} for each cell is given by:

$$i_{L1,j}^{\delta\in\{0,1\}}(k+1) = i_{L1,j}(k) + \frac{T_S}{L_{1,j}}\begin{bmatrix} v_{PV,j}(k) - \delta \times v_{C1,j}(k) \\ +(1-\delta)\times v_{C2,j}(k)\end{bmatrix} \tag{7}$$

where j denotes the qZSI cell number, $i_{L1,j}^{\delta\in\{0,1\}}(k+1)$ is the cell j input inductor current predition and δ is non-shoot-through indicator, i.e. δ is equal to zero in shoot-through mode.

B. REFERENCE SIGNAL GENERATION

The proposed MPC scheme includes three references: input inductor current of cell 1 qZSI ($i_{L1,1}$), input inductor current of cell 2 qZSI ($i_{L1,2}$), and injected current to the grid (i_a). As shown in section II.C, the reference signals for $i_{L1,1}$and $i_{L1,2}$ are generated by the MPPT algorithm based on the power extraction requirement and grid condition. Furthermore, the grid current reference is generated by its two quadrature components i.e. d component for the real power and q component for the reactive power injection respectively. The total grid current d-component (real power) is calculated via separate PI controllers for both qZS cells; these PI controllers generate the active current references (d-component) by regulating the $V_{C1,1}$ and $V_{C1,2}$ voltages of qZSI cells. The reference for $V_{C1,1}$ and $V_{C1,2}$ voltages is 150V, adding up to over twice the grid voltage having $120V_{rms}$ to fulfill high demand of reactive power. The q-component is given by the grid codes as explained in sections I and II based on the amount of grid voltage sag [29], [31]. Finally, these d and q current references with angle information from PLL will be converted into (8), which is the AC grid current reference for the MPC controller.

$$i_{a,ref} = i_{d,ref}\sin(\omega t) + i_{q,ref}\cos(\omega t) \tag{8}$$

TABLE 2. Switching states for the qZS-CMI.

Switching States	S_a	S_{an}	S_b	S_{bn}	S_c	S_{cn}	S_d	S_{dn}	Cell 1 Output Voltage	Cell 2 Output Voltage
1	0	1	0	1	0	1	0	1	0 (Z)	0 (Z)
2	0	1	0	1	1	0	1	0	0 (Z)	0 (Z)
3	0	1	1	0	1	0	1	0	$-V_{DC,1}$	0 (Z)
4	1	0	0	1	0	1	1	0	$+V_{DC,1}$	$-V_{DC,2}$
5	1	0	1	0	0	1	0	1	0 (Z)	0 (Z)
6	1	0	1	0	1	0	1	0	0 (Z)	0 (Z)
7	0	1	0	1	0	1	1	0	0 (Z)	$-V_{DC,2}$
8	0	1	1	0	0	1	0	1	$-V_{DC,1}$	0 (Z)
9	0	1	1	0	1	0	1	0	$-V_{DC,1}$	0 (Z)
10	1	0	1	0	0	1	1	0	0 (Z)	$-V_{DC,2}$
11	0	1	0	1	1	0	0	1	0 (Z)	$+V_{DC,2}$
12	1	0	0	1	0	1	0	1	$+V_{DC,1}$	0 (Z)
13	1	0	0	1	1	0	1	0	$+V_{DC,1}$	0 (Z)
14	1	0	1	0	1	0	0	1	0 (Z)	$+V_{DC,2}$
15	0	1	1	0	0	1	1	0	$-V_{DC,1}$	$-V_{DC,2}$
16	1	0	0	1	1	0	0	1	$+V_{DC,1}$	$+V_{DC,2}$
17	1	1	0	1	1	0	0	1	0 (ST)	$+V_{DC,2}$
18	1	0	0	1	1	1	0	1	$+V_{DC,1}$	0 (ST)
19	1	1	0	1	1	1	0	1	0 (ST)	0 (ST)
20	1	1	0	1	0	1	1	0	0 (ST)	$-V_{DC,2}$
21	0	1	1	0	1	1	0	1	$-V_{DC,1}$	0 (ST)
22	1	1	0	1	0	1	0	1	0 (ST)	0 (Z)
23	1	1	0	1	1	0	1	0	0 (ST)	0 (Z)
24	0	1	0	1	1	1	0	1	0 (Z)	0 (ST)
25	1	0	1	0	1	1	0	1	0 (Z)	0 (ST)

Z: Zero state, ST: Shoot-Through state

IV. EFFICIENT CONTROLLER AND STABILITY ANALYSIS

All feasible switching states of the qZS-CMI are listed in Table II for prediction of control objectives. These include all active, zero, and shoot-through states. The control scheme takes advantage of the cost redundancy of the $i_{L1}(k+1)$ predictions, as the predictions are equal for all switching states except shoot-through. In this section, i_{L1} next-state

predictions for shoot-through and non-shoot-through modes will be referred to as ${i_{L1}}^{ST}(k+1)$ and ${i_{L1}}^{NST}(k+1)$, respectively, for clarity and conciseness. The control algorithm is discussed in more detail in the following subsections.

A. VOLTAGE WINDOW

When implementing a multilevel inverter, it is preferable to reduce harmonic content of the output voltage without interfering with grid current optimization. This is achieved by applying a *voltage window* for each switching state. This control will only consider voltage levels within one step of the previous output voltage level. This has the added benefit of reducing the number of switching considerations. The voltage window is applied by using the selected switching state as a feedback to the controller, to determine which voltage levels can be considered for the following time step.

B. COST PACKAGE CONSTRUCTION

For every time step, one cost package is constructed for each qZS cell and sent to the supervisory controller. The cost packages contain all needed information for the supervisory controller to automatically filter out switching states that are unable to optimize the input current objective or adhere to the voltage window. The cost packages and previous output voltage constitute the addresses of associated reduced optimization sets. Algorithm 1 evaluates the cost of the i_{L1} objectives for both ST and NST scenarios. The cost packages rank each scenario by row and contains the cost of each scenario in the second column. In most cases, the grid current optimizer only needs to know which state should be implemented for i_{L1} optimization, but knowing the control cost of the second-rank objective is needed when i_{L1} optimization and the voltage window constraint conflict, as is explained in the following subsection.

C. EFFICIENT SUPERVISORY PREDICTIVE CONTROL

The control algorithm uses the previous voltage level and the input current control objective to filter out several switching states. Fig. 3 outlines the supervisory control algorithm, and it specifies the switching states that are remaining to optimize injected grid current. The control paths all differ to satisfy the voltage window and i_{L1} control constraints. For example, consider the scenario when the previous output voltage was $+2V_{DC}$ and Algorithm 1 has determined both input currents are optimized in the non-shoot-through state. The shoot-through switching states must be eliminated. Additionally, to satisfy the voltage window constraint, only the switching states which produce $+V_{DC}$ or $+2V_{DC}$ can be considered. Thus, the remaining switching states available for grid current optimization are limited to states 11-14 and 16, which produce an output voltage of $+V_{DC}$ and $+2V_{DC}$, respectively. Now consider a similar scenario, except Algorithm 1 has determined that cell 1 must implement shoot-through for $i_{L1,1}$ optimization. To allow for shoot-through of cell 1 and adhere to the voltage window constraint, a positive DC-link voltage level must be applied across cell 2; state 17 is the only

Algorithm 1 Cost Package Construction

Function [CP_1, CP_2] = CP_Contsruct ($v_{c1\&2}(k)$, $I_{PV1\&2}(k)$, $i_{L1,1\&2ref}(k)$)

Initialization: sampling at $\mathrm{T_s}$

1: Find input current costs for each cell

Finding predicted i_{L1} in next state for each cell:

$\delta = 1$, indicating non-shoot-through (NST) mode

${i_{L1,1}}^{\mathrm{NST}}(k+1)$ and ${i_{L1,2}}^{\mathrm{NST}}(k+1) \leftarrow$ compute from (6)

$\delta = 0$, indicating shoot-through (ST) mode

${i_{L1,1}}^{\mathrm{ST}}(k+1)$ and ${i_{L1,2}}^{\mathrm{ST}}(k+1) \leftarrow$ compute from (6)

Finding i_{L1} costs for each control action:

$g_{NST,1} = |{i_{L1,1}}^{NST}(k+1) - i_{L1,1ref}(k)|$

$g_{ST,1} = |{i_{L1,1}}^{ST}(k+1) - i_{L1,1ref}(k)|$

$g_{NST,2} = |{i_{L1,2}}^{NST}(k+1) - i_{L1,2ref}(k)|$

$g_{ST,2} = |{i_{L1,2}}^{ST}(k+1) - i_{L1,2ref}(k)|$

2: Construct Cost Package for each cell

if $(g_{ST,1} < g_{NST,1})$

$$\mathrm{CP}_1 = \begin{bmatrix} \text{'}ST\text{'} & g_{ST,1} \\ \text{'}NST\text{'} & g_{NST,1} \end{bmatrix}$$

else

$$\mathrm{CP}_1 = \begin{bmatrix} \text{'}NST\text{'} & g_{NST,1} \\ \text{'}ST\text{'} & g_{ST,1} \end{bmatrix}$$

end if

if $(g_{ST,2} < g_{NST,2})$

$$\mathrm{CP}_2 = \begin{bmatrix} 'ST' & g_{ST,2} \\ 'NST' & g_{NST,2} \end{bmatrix}$$

else

$$\mathrm{CP}_2 = \begin{bmatrix} 'NST' & g_{NST,2} \\ 'ST' & g_{ST,2} \end{bmatrix}$$

end if

Return CP_1, CP_2

end function

state that satisfies both conditions. Thus, state 17 is chosen automatically, with grid current optimization bypassed.

There is one scenario in which the voltage window and input current control objectives cannot be met simultaneously. This occurs when ${v^{ML}}_{qZSI}(k)$ is equal to $\pm 2V_{DC}$, and both i_{L1} objectives are optimized by implementing shoot-through. This is because the DC-link voltage is zero when both cells are in shoot-through, which is not within the voltage window for ${v^{ML}}_{qZSI}(k)$ equal to $\pm 2V_{DC}$. Adhering to both i_{L1} objectives would violate the voltage window constraint, as the output voltage would be zero. To address this, the controller must decide which $\mathrm{i_{L1}}$ objective should be defied. The decision is made by comparing the second-rank cost of each qZS cell, and the cell with the highest rank cost implements shoot-through. That is, the cell with its input current objective more closely optimized in non-shoot-through will defy its i_{L1} objective. As shown in Fig. 3, the second-row, second-column element of both cost packages are compared, and the cell with the highest second-rank cost implements shoot-through.

D. COMPARISON WITH TRADITIONAL FINITE-SET MPC

For the proposed system, traditional finite-set MPC considers 5^N switching states for every time step, where the system has

TABLE 3. Cost computation comparison.

Considered Control Path	i_{L1} Cost Computations	i_a Cost Computations	Overall Cost Function Computations	Total Cost Computations	Comp. Reduction from Traditional FS-MPC
Lowest Comp. path	4	0	0	4	96%
Highest Comp. path	4	14	0	18	82%
Average for all paths	4	3.3	0	7.3	92.7%
Traditional FS-MPC	50	25	25	100	0%

N qZS cells. To optimize the same control objectives as in the proposed control, the cost function is:

$$\begin{aligned} g = \lambda_1 \left\| I_{L1,1\text{ref}}(k) - I_{L1,1}(k+1) \right\| \\ + \lambda_2 \left\| I_{L1,2ref}(k) - I_{L1,2}(k+1) \right\| \\ + \lambda_3 \left\| i_{a,ref}(k) - i_a(k+1) \right\| \end{aligned} \tag{9}$$

where the λ_{1-3} are scaling terms, commonly referred to as weight factors. Using this control approach would require preliminary design of the weight factors. As shown in Table III, the cost computations required for this control scheme is $5^N(\beta+1)$, where β is the number of control objectives. For the proposed five-level qZS-CMI, traditional finite-set MPC requires 100 cost function computations. In the proposed control, the number of cost computations is dependent on the cost packages and the previous voltage state. As shown in Fig. 3, there are $N^2(2N+1)$ control paths for the proposed controller, which can vary in the number of necessary switching states to consider for grid current optimization. In the proposed scheme, half of the control paths do not require any optimization. As shown in Table III, these iterations require only four cost computations, which are necessary to develop the cost packages. The control path with the most cost computations needed is the case where the previously implemented output voltage was zero and both i_{L1} objectives are optimized in the non-shoot-through state. Table III shows the average control path has over a ninety percent reduction in cost computation. It is notable that no functionality is lost in this architecture, as it only exploits cost redundancy of the input current predictive model, and applies higher priority to input current, as is typically done in predictively controlled quasi-Z-source inverters.

E. STABILITY ANALYSIS

Stability of the system is investigated by means of the Lyapunov stability analysis. The next-state converter output voltage ${v^{ML,opt}}_{qZSI}(k+1)$ necessary for optimal tracking is represented by:

$$v^{ML}_{qZSI}(k+1) = v^{ML,opt}_{qZSI}(k+1) + \phi(k+1) \tag{10}$$

Here, ${v^{ML}}_{qZSI}(k+1)$ is the CMI output voltage from the executable switching states, ${v^{ML,opt}}_{qZSI}(k+1)$ is the output voltage that will produce zero error in grid current in the following time step, and output voltage quantization error is defined as $\phi(k+1)$. In this case, the magnitude of $\phi(k+1)$ is less than or equal to l, where $l \epsilon R^+$. Since ${v^{ML}}_{qZSI}(k+1)$ is within a finite set and remains bounded, the hysteresis

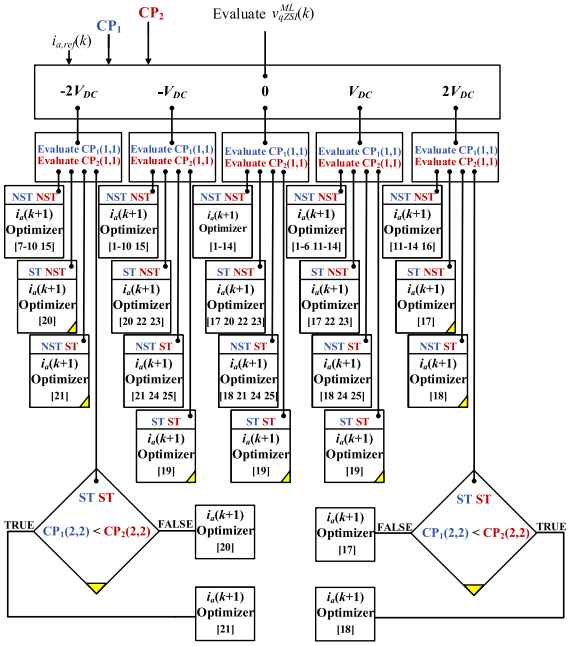

FIGURE 3. Control paths of embedded switching state screen (yellow triangle in path denotes that no grid current optimization is needed).

bounds with length $\phi(k+1)$ must be bounded also, and therefore 'l' is certain to exist. Using the system parameters defined previously, the error in grid-side current is defined as:

$$i_{a,err} = i_a(k+1) - i_{a,ref}(k+1) \tag{11}$$

Using (6):

$$\begin{aligned} i_{a,err}(k+1) = i_a(k)\left[1 - \frac{R}{L}T_S\right] + \frac{T_S}{L}\left[v^{ML}_{qZSI}(k) - e_a(k)\right] \\ - i_{a,ref}(k+1) \end{aligned} \tag{12}$$

The objective of the control is to diminish tracking error $i_{a,err}$ asymptotically to zero or to a miniscule error tolerance. The Lyapunov function $L(k)$ is defined as:

$$L\left(i_{a,err}\right) = \frac{1}{2}\left[i_{a,err}(k)\right]^2 \tag{13}$$

From Lyapunov theorem, the time derivative of the Lyapunov function $\Delta L(i_{a,err})$ must always be negative for the convergence of $i_{a,err}$ to zero and for system stability. Thus, $i_{a,err}$ will tend to zero if and only if $\Delta L(i_{a,err}) < 0$. Using (12),

the time derivative of the Lyapunov function is defined as:

$$\Delta L\left(i_{a,err}\right) = L\left(i_{a,err}(k+1)\right) - L\left(i_{a,err}(k)\right)$$

$$\Delta L\left(i_{a,err}\right) = \frac{1}{2}\left[\begin{array}{l} i_a(k)\left[1-\frac{R}{L}T_S\right]+\frac{T_S}{L} \\ \times\left(v^{ML}_{qZSI}(k)+\phi(k+1)-e_a(k)\right) \\ -i_a(k+1)\end{array}\right]^2 - \left(\frac{1}{2}\right)\left[i_{a,er}(k)\right]^2 \quad (14)$$

The discrete future voltage vector that ensures a negative time derivative of $\Delta L(i_{a-error})$ is defined as:

$$v^{ML}_{qZSI} = \frac{L}{T_S}i_a(k+1) + i_a(k)\left[R-\frac{L}{T_S}\right] + e_a(k) \quad (15)$$

For Lyapunov stability, the system should meet the following criteria:

$$\begin{aligned} &L\left(i_{a-\text{error}}(k)\right) \geq C_1\left|i_{a-\text{error}}(k)\right|^{\sigma}, \quad \forall i_{a-\text{error}}(k) \in \Upsilon \\ &L\left(i_{a-\text{error}}(k)\right) \geq C_2\left|i_{a-\text{error}}(k)\right|^{\sigma}, \quad \forall i_{a-\text{error}}(k) \in \Gamma \\ &L\left(i_{a,\text{err}}(k+1)\right) - L\left(i_{a,\text{err}}(k)\right) \\ &\qquad < -C_3\left|i_{a,\text{err}}(k)\right|^{\sigma} + C_4 \\ &\qquad\quad C_1, C_2, C_3, C_4 \in \mathbb{R}^+, \quad \sigma \geq 1 \\ &\qquad\quad \Upsilon \in \mathbb{R}^+, \quad \Gamma \subset \Upsilon \end{aligned} \quad (16)$$

Substituting (15) into (14):

$$\frac{1}{2}\left(\frac{T_S}{L}\right)^2 l^2 - \frac{1}{2}\left[i_{a-\text{error}}(k)\right]^2 \geq \Delta L(k) \quad (17)$$

Additionally, the grid-side current vector converges to a condensed equation:

$$\Omega = \left\{\left\|i_{a-\text{error}}(k)\right\|^2 \leq \frac{T_S}{L}l\right\} \quad (18)$$

From (16),

$$C_1 = C_2 = 1, \quad C_3 = \frac{1}{2}, \quad C_4 = \frac{1}{2}\left[\frac{L}{T_S}\right]^2 l^2$$

Thus, controlled parameters are within a bounded region, and therefore satisfy Lyapunov's stability criterion.

V. RESULTS AND DISCUSSIONS

The performance of the proposed control scheme is tested during solar irradiance transients and grid voltage sags. Each RPI strategy presented in section II is showcased. The experiments are implemented with the dSPACE MicrolabBox control platform. A qZS-CMI with two 1kW PV modules connected to each inverter cell is used for the case studies. An RPI ramping rate of 2 p.u. is implemented for the case studies in each scenario, where reactive current saturates at $16.7A_{RMS}$ for a fifty percent voltage sag. Additional system specifications are provided in Table IV. For each LVRT mode case study, a 20% grid voltage sag is induced, and the RPI is increased to 0.64kVAR, while active power injection varies for each RPI strategy. The major evaluation criteria considered in the case studies are: a) ability to adjust active and reactive power injection to the grid according to the desired RPI strategy during LVRT mode; b) seamless transition between LVRT and normal grid modes of operation; c) ability to operate at global MPP with mismatch in PV modules i.e. unbalance solar irradiance of PV modules connected to different qZSI cell.

TABLE 4. System specifications.

Parameter	Value
Sampling Time	20µs
Filter Inductance	4mH
DC Filter Resistance	50mΩ
Impedance Network Inductances	1.5mH
Impedance Network Capacitances	1000µF
Input Capacitance	2200µF
P_{MPP}	1000W
V_{MPP}	85.6V
Rated Grid Voltage	$120V_{RMS}$

Fig. 4-Fig. 6 show the system dynamics response to grid voltage sag for average active power, constant peak current, and constant active current control strategies respectively. The grid-side voltage and current, $i_{L1,1}$, and $v^{ML}{}_{qZSI}$ are captured for these case studies. In Fig. 4, a 20% voltage sag is triggered at t_1, transitioning the control from MPPT to the constant average active power LVRT mode. The inductor current $i_{L1,1}$ is shown to remain constant after the voltage sag trigger, showing that the average active power injection of roughly 2kW remains constant. The MPPT algorithm of each cell's PV array remains at its MPP. Additionally, the grid voltage sag and resultant $i_{q,ref}$ creates a voltage swell across the DC link, shown in Fig. 4b. A voltage swell is also seen across both $C_{1,1}$and $C_{1,2}$. The PI controller responds by increasing the active current component $i_{d,ref}$ from 20.6A to about 26.8A, and the DC link voltage returns to 400v. Thus, grid-side current amplitude increases with the voltage sag to maintain constant active power as well as inject reactive power. The FFT plot of injected current during the sag is shown in Fig. 4c. The measured THD is 1.61%, well within the IEEE-519 standard of 5% [32]. Fig. 5 shows the constant peak current control strategy when the voltage sag occurs at t_2. The injected active power decreases to about 1.32kW according to (4). The reduction in power extraction from the PV arrays causes a reduction in DC link voltage, as shown in Fig. 5b. Consequently, a voltage reduction is seen across $C_{1,1}$ and $C_{1,2}$. The PI controller reduces $i_{d,ref}$ to about 18.9A to return DC link voltage to normal condition. Grid current peak remains constant during voltage sag, but the grid current leads the voltage after instant t_2 while i_{L1} decreases. This indicates that the required reactive power is injected, while active power decreases according to constant peak current strategy. The FFT plot for the injected current during the

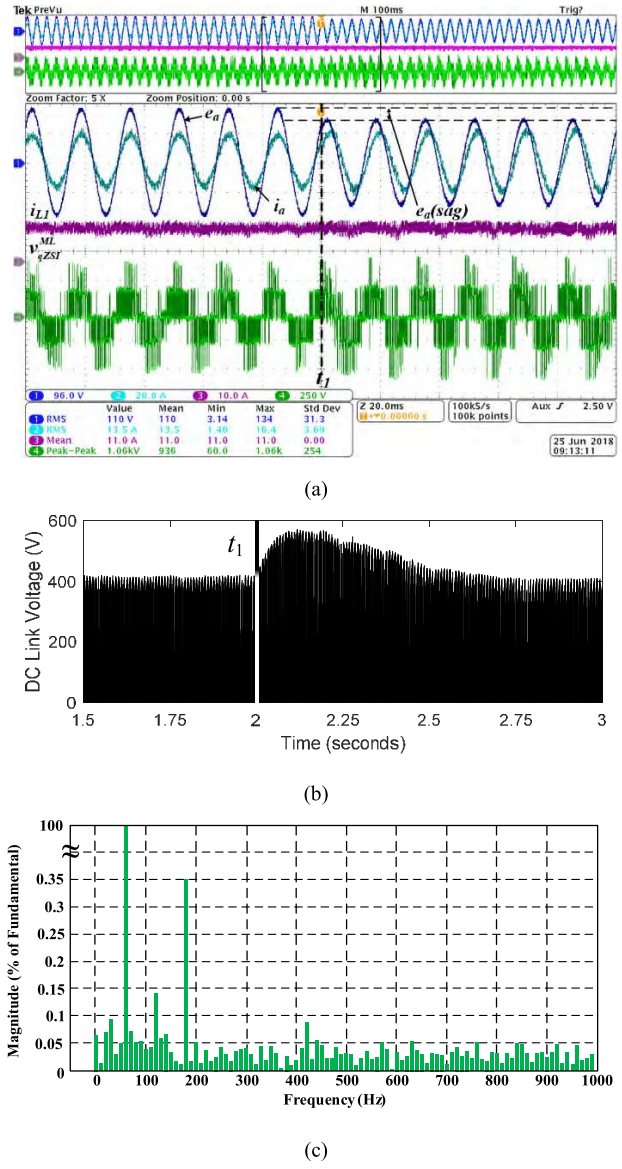

FIGURE 4. Constant average active power control strategy, grid voltage sag occurred at t1. Grid voltage, injected grid current, qZS cell 1 input current and output voltage (a). DC link voltage (b). FFT plot of injected current 500ms after voltage sag transient; THD of 1.61% is measured (c).

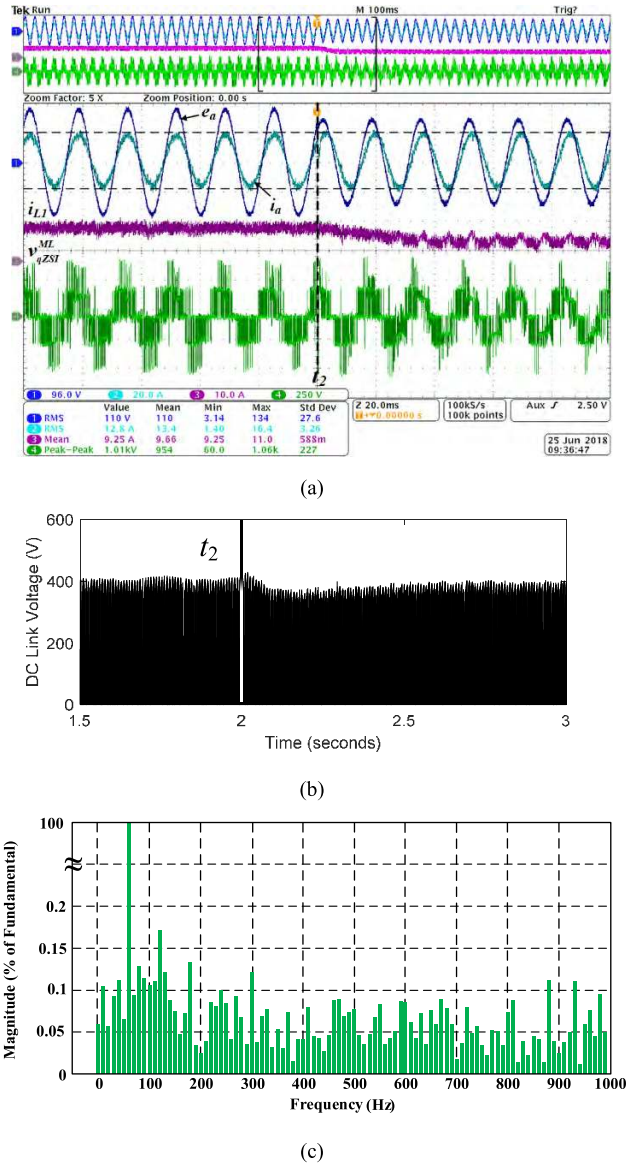

FIGURE 5. Constant peak current control strategy, grid voltage sag occurred at t1. Grid voltage, injected grid current, qZS cell 1 input current and output voltage (a). DC link voltage (b). FFT plot of injected current 500ms after voltage sag transient; THD of 2.65% is measured (c).

voltage sag is shown in Fig. 5c. An increase in THD is noted when compared to the constant average active power RPI strategy, due to the change in the grid current magnitude. Fig. 6 shows RPI for constant active current after a voltage sag occurs at t_3, where a reduction in $i_{L1}$is seen according to this RPI strategy. For this RPI strategy, active power injection decreases to 1.6kW. The MPPT algorithm of each qZS cell moves the PV operation point to right of the MPP, until reaching a power limit of 800W. The reduced power extraction from the PV arrays and the reactive power injection counteract their effects on the DC link voltage, and thus no transient is seen in the DC link voltage, as shown in Fig. 6b. Thus, the voltage across $C_{1,1}$ and $C_{1,2}$ is maintained, and $i_{d,ref}$ is unchanged. Therefore, applying (2) to the MPPT algorithm successfully maintains the active current injection during grid voltage transients. The FFT plot of grid current is shown in Fig. 6c. The measured THD is lower compared with the constant peak current strategy, due to larger grid current amplitude. For each FFT plot, it is noteworthy that the FFT analysis shows a uniform distribution of harmonic content across the frequency spectrum; this is a result of the variable switching frequency inherent to finite-set MPC In Fig. 7, the grid recovers from voltage sag at t_4, transitioning rapidly from average active power strategy in LVRT to MPPT mode. This is evidenced by the reduction in grid-side current amplitude and the phase alignment of grid-side current and voltage after t_4. These experiments verify the controller performance based on aforementioned evaluation criteria (a) and (b).

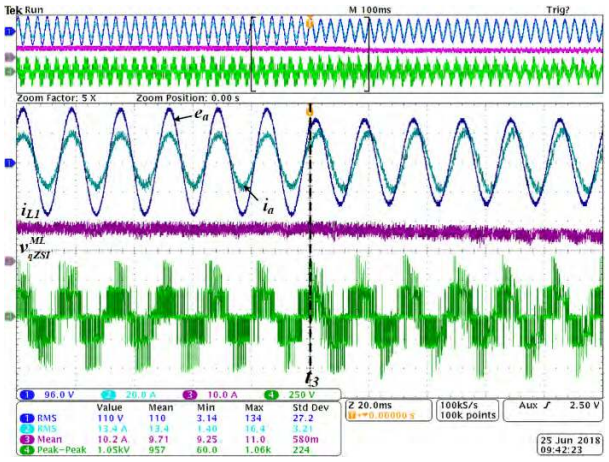

(a)

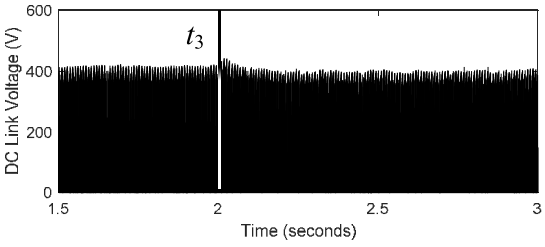

(b)

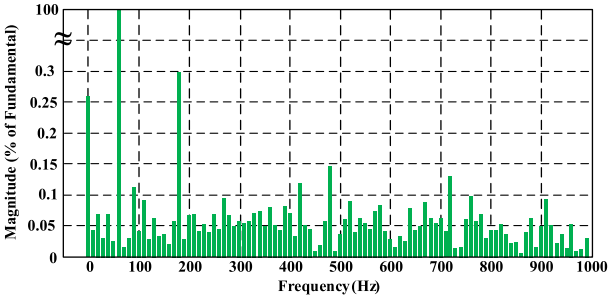

(c)

FIGURE 6. Constant active current control strategy, grid voltage sag occurred at t1. Grid voltage, injected grid current, qZS cell 1 input current and output voltage (a). DC link voltage (b). FFT plot of injected current 500ms after voltage sag transient; THD of 2.46% is measured (c).

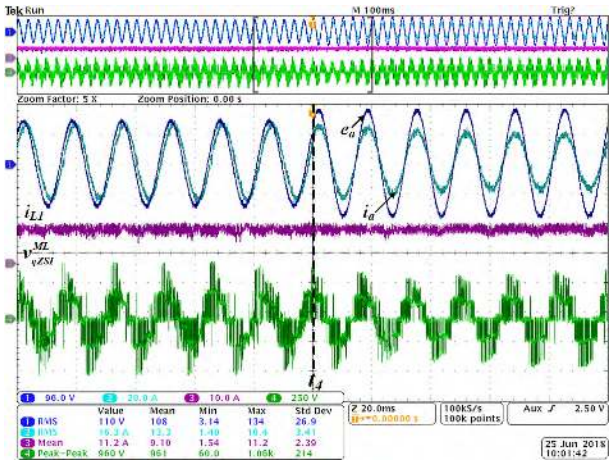

FIGURE 7. System recovery from LVRT to normal grid conditions at instant t_4 using constant average active power control strategy.

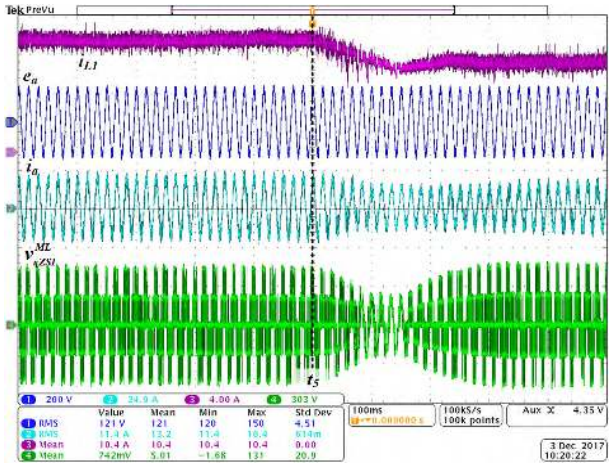

FIGURE 8. Step change in solar irradiance from 1000W/m^2 to 800W/m^2 at instant t_5 in normal grid mode.

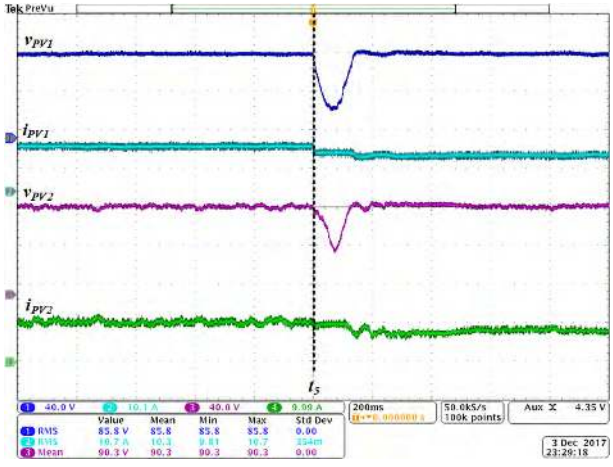

FIGURE 9. PV-side parameters during a step change in solar irradiance from 1000W/m^2 to 800W/m^2 at instant t_5 in normal grid mode.

Fig. 8 shows grid-side parameters during a step change in solar irradiance from 1000W/m^2 to 800W/m^2 at t_5 in normal grid mode. The reduction in power to the grid causes a sag in DC link voltage, and the PI controller responds by reducing $i_{d,ref}$. Fig. 9 shows the PV-side parameters for the step-change in solar irradiance at instant t_5. As it is captured, the PV current and voltage adjusted to track the new MPP in less than 180ms after the transient occurred at t_5, this case study demonstrates the fast-dynamic response of the proposed control scheme to step change in solar irradiance.

Finally, the system is tested under PV mismatching conditions to verify the controller performance according to aforementioned evaluation criteria (c). In Fig. 10 at t_6, the solar irradiance of the PV string connected to the qZSI cell 1 is reduced from 1000W/m^2 to 800W/m^2, while the PV string of the qZSI cell 2 operates at 1000W/m^2. The grid-side peak

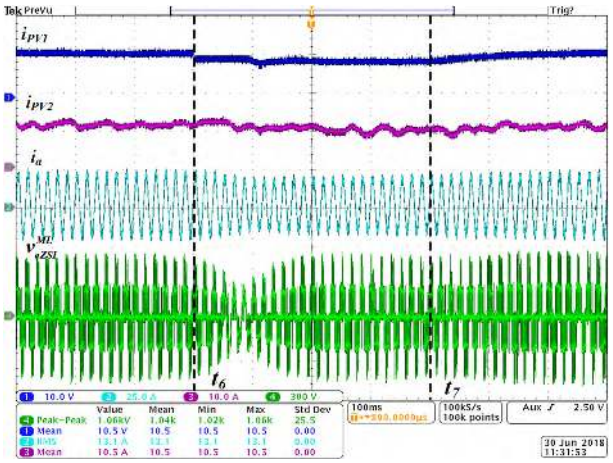

FIGURE 10. PV mismatching due to unbalance solar irradiance level of PV cells, transient from 1000W/m^2 to 800W/m^2 in solar irradiance of PV cell 1 during period t_6 to t_7 while the solar irradiance of PV cell 2 is kept constant at 1000W/m^2.

current and PV string 1 current, i_{PV1}, are reduced according to the new MPP operation, while the PV string 2 current is maintained according to its MPP operation at 1000 W/m^2. The solar irradiance of PV string 1 returns to 1000W/m^2 at t_7. This case study demonstrates the robustness of the proposed control scheme to unbalance solar irradiance at cells of qZSI-CMI. As it is shown, each qZSI cell can independently boost its voltage, making the inverter more robust and preventing uneven voltage levels. The system maintains stability during PV string mismatch conditions.

VI. CONCLUSION

A power electronics interface and control scheme for a cascaded multilevel impedance-source inverter is presented in this paper. It is capable of operating each PV string independently and employs RPI during abnormal grid conditions to support grid stability. The efficient control scheme reduces over ninety percent of the cost computation on average, when compared to a finite-set MPC scheme with the same control objectives. With the decoupled active and reactive power control, the proposed system can support unity power factor of the grid during voltage sags. Additionally, the system is shown to remain stable during solar irradiance imbalances and transients in solar irradiance.

REFERENCES

[1] S. B. Kjaer, J. K. Pederson, and F. Blaabjerg, "A review of single-phase grid-connected inverters for photovoltaic modules," *IEEE Trans. Ind. Appl.*, vol. 41, no. 5, pp. 1292–1306, Sep./Oct. 2005.

[2] Y. Liu, B. Ge, H. Abu-Rub, and H. Sun, "Hybrid pulsewidth modulated single-phase quasi-Z-source grid-tie photovoltaic power system," *IEEE Trans. Ind. Informat.*, vol. 12, no. 2, pp. 621–632, Apr. 2016.

[3] M. Mirhosseini, J. Pou, and V. G. Agelidis, "Single- and two-stage inverter-based grid-connected photovoltaic power plants with ride-through capability under grid faults," *IEEE Trans. Sustain. Energy*, vol. 6, no. 3, pp. 1150–1159, Jul. 2015.

[4] Y. Zhu and J. Fei, "Disturbance observer based fuzzy sliding mode control of PV grid connected inverter," *IEEE Access*, vol. 6, pp. 21202–21211, 2018.

[5] Y. Zhu and J. Fei, "Adaptive global fast terminal sliding mode control of grid-connected photovoltaic system using fuzzy neural network approach," *IEEE Access*, vol. 5, pp. 9476–9484, 2017.

[6] B. Xu and X. Ran, "Sliding mode control for three-phase quasi-Z-source inverter," *IEEE Access*, vol. 6, pp. 60318–60328, 2018.

[7] S. Sabyasachi, V. B. Borghate, R. R. Karasani, S. K. Maddugari, and H. M. Suryawanshi, "Hybrid control technique-based three-phase cascaded multilevel Inverter topology," *IEEE Access*, vol. 5, pp. 26912–26921, 2017.

[8] Y. Liu, B. Ge, H. Abu-Rub, and F. Z. Peng, "An effective control method for three-phase quasi-Z-source cascaded multilevel inverter based grid-tie photovoltaic power system," *IEEE Trans. Ind. Electron.*, vol. 61, no. 12, pp. 6794–6802, Dec. 2014.

[9] X. Yuan, J. Chai, and Y. Li, "A transformer-less high-power converter for large permanent magnet wind generator systems," *IEEE Trans. Sustain. Energy*, vol. 3, no. 3, pp. 318–329, Jul. 2012.

[10] Y. Liu, B. Ge, H. Abu-Rub, and F. Z. Peng, "Control system design of battery-assisted quasi-Z-source inverter for grid-tie photovoltaic power generation," *IEEE Trans. Sustain. Energy*, vol. 4, no. 4, pp. 994–1001, Oct. 2013.

[11] H. Abu-Rub, A. Iqbal, S. M. Ahmed, F. Z. Peng, Y. Li, and G. Baoming, "Quasi-Z-source inverter-based photovoltaic generation system with maximum power tracking control using ANFIS," *IEEE Trans. Power Electron.*, vol. 4, no. 1, pp. 11–20, Jan. 2013.

[12] B. Ge, F. Z. Peng, H. Abu-Rub, F. J. T. E. Ferreira, and A. T. de Almeida, "Novel energy stored single-stage photovoltaic power system with constant DC-link peak voltage," *IEEE Trans. Sustain. Energy*, vol. 5, no. 1, pp. 28–36, Jan. 2014.

[13] U. K. Shinde, S. G. Kadwane, S. P. Gawande, M. J. B. Reddy, and D. K. Mohanta, "Sliding mode control of single-phase grid-connected quasi-Z-source inverter," *IEEE Access*, vol. 5, pp. 10232–10240, 2017.

[14] B. Ge, Y. Liu, H. Abu-Rub, and F. Z. Peng, "State-of-charge balancing control for a battery-energy-stored quasi-Z-source cascaded-multilevel-inverter-based photovoltaic power system," *IEEE Trans. Ind. Electron.*, vol. 65, no. 3, pp. 2268–2279, Mar. 2018.

[15] J. Anderson and F. Z. Peng, "Four quasi-Z-source inverters," in *Proc. IEEE 39th Annu. PESC*, Rhodes, Greece, Jun. 2008, pp. 2743–2749.

[16] Y. Liu, H. Abu-Rub, and B. Ge, "Z-source/quasi-Z-source inverters: Derived networks, modulations, controls, and emerging applications to photovoltaic conversion," *IEEE Ind. Electron.Mag.*, vol. 8, no. 4, pp. 32–44, Dec. 2014.

[17] A. Ayad, P. Karamanakos, and R. Kennel, "Direct model predictive current control strategy of quasi-Z-source inverters," *IEEE Trans. Power Electron.*, vol. 32, no. 7, pp. 5786–5801, Jul. 2016.

[18] Y. Shan, J. Hu, K. W. Chan, Q. Fu, and J. M. Guerrero, "Model predictive control of bidirectional DC-DC converters and AC/DC interlinking converters—A new control method for PV-wind-battery microgrids," *IEEE Trans. Sustain. Energy*, to be published.

[19] P. Cortés *et al.*, "Guidelines for weighting factors design in model predictive control of power converters and drives," in *Proc. IEEE ICIT*, Churchill, VIC, Australia, Feb. 2009, pp. 1–7.

[20] Y. Liu, H. Abu-Rub, B. Ge, F. Blaabjerg, O. Ellabban, and P. C. Loh, *Impedance Source Power Electronic Converters*. Hoboken, NJ, USA: Wiley, 2016.

[21] D. Sun, B. Ge, W. Liang, H. Abu-Rub, and F. Z. Peng, "An energy stored quasi-Z-source cascade multilevel inverter-based photovoltaic power generation system," *IEEE Trans. Ind. Electron.*, vol. 62, no. 9, pp. 5458–5467, Sep. 2015.

[22] D. Sun *et al.*, "Modeling, impedance design, and efficiency analysis of quasi-Z source module in cascaded multilevel photovoltaic power system," *IEEE Trans. Ind. Electron.*, vol. 61, no. 11, pp. 6108–6117, Nov. 2014.

[23] M. Aleenejad and R. Ahmadi, "Fault-tolerant multilevel cascaded H-bridge inverter using impedance-sourced network," *IET Power Electron.*, vol. 9, no. 11, pp. 2186–2195, 2016.

[24] M. Trabelsi, S. Bayhan, H. Abu-Rub, L. Ben-Brahim, and P. Zanchetta, "Finite control set model predictive control for grid-tied quasi-Z-source based multilevel inverter," in *Proc. IEEE ICIT*, Taipei, Taiwan, Mar. 2016, pp. 299–304.

[25] E. On, "Grid code high and extra high voltage," E. On Netz Gmbh, Bayreuth, Germany, Tech. Rep., 2006.

[26] C. C. Hua, C. W. Wu, and C. W. Chuang, "A Digital predictive current control with improved sampled inductor current for cascaded inverters," *IEEE Trans. Ind. Electron.*, vol. 56, no. 5, pp. 1718–1726, May 2009.
[27] M. A. Perez, P. Cortes, and J. Rodriguez, "Predictive control algorithm technique for multilevel asymmetric cascaded H-bridge inverters," *IEEE Trans. Ind. Electron.*, vol. 55, no. 12, pp. 4354–4361, Dec. 2008.
[28] P. Cortes, A. Wilson, S. Kouro, J. Rodriguez, and H. Abu-Rub, "Model predictive control of multilevel cascaded H-bridge inverters," *IEEE Trans. Ind. Electron.*, vol. 57, no. 8, pp. 2691–2699, Aug. 2010.
[29] Y. Yang, H. Wang, and F. Blaabjerg, "Reactive power injection strategies for single-phase photovoltaic systems considering grid requirements," *IEEE Trans. Ind. Appl.*, vol. 50, no. 6, pp. 4065–4076, Nov./Dec. 2014.
[30] M. Ciobotaru, R. Teodorescu, and F. Blaabjerg, "A new single-phase PLL structure based on second order generalized integrator," in *Proc. 7th IEEE PESC*, Jeju, South Korea, Jun. 2006, pp. 1–6.
[31] C.-Y. Tang, Y.-T. Chen, and Y.-M. Chen, "PV power system with multi-mode operation and low-voltage ride-through capability," *IEEE Trans. Ind. Electron.*, vol. 62, no. 12, pp. 7524–7533, Dec. 2015.
[32] *IEEE Recommended Practices and Requirements for Harmonic Control in Electrical Power Systems*, Standard 519-1992, I. F II, New York, NY, USA, 1993.

MITCHELL EASLEY (S'18) received the B.S. degree in electrical engineering from Kansas State University, Manhattan, KS, in 2018, where he is currently pursuing the M.S. degree with the Department of Electrical and Computer Engineering.

Since 2017, he has been a Research Associate with the Power Electronics and Autonomous Systems Research Laboratory, Kansas State University. His current research interests include model predictive control, wide bandgap-based power converters, and multilevel converters.

SARTHAK JAIN received the B.Tech. degree in electrical engineering from GGSIPU, New Delhi, India, in 2014, and the M.S. degree in electrical engineering from Texas A&M University, College Station, TX, in 2018.

He was a Research Associate with Delhi Technological University, New Delhi, from 2014 to 2016, and the Renewable Energy and Advanced Power Electronics Laboratory, College Station, from 2016 to 2017. He is currently an Application Engineer with the Core Power Solutions Group, Renesas Electronics America, Milpitas, CA. His current research interests include PV grid tied inverters and dc/dc resonant converters.

MOHAMMAD B. SHADMAND (S'09–M'15) received the Ph.D. degree in electrical engineering from Texas A&M University, College Station, TX, USA, in 2015.

From 2015 to 2016, he was an Instructor with the Department of Electrical and Computer Engineering, Texas A&M University. From 2016 to 2017, he was a Research Engineer with the Renewable Energy and Advanced Power Electronics Research Laboratory, TX, USA. He is currently an Assistant Professor with the Department of Electrical and Computer Engineering and the Co-Director of the Power Electronics and Autonomous Systems (PEAS) Research Laboratory, Kansas State University, Manhattan, KS, USA. He has published more than 50 journal and conference papers. His current research interests include advanced model predictive control, grid-tied power electronics interfaces with advance functionalities, matrix converter, and control of smart microgrid systems.

Dr. Shadmand was awarded with the Second Place at the IEEE Industrial Application Society Graduate Thesis Contest, in 2013. He received the IEEE Standard Education Award for the project Fixed-Step Model Predictive Control of Grid-Tied Photovoltaic Inverter, in 2014. He was also awarded with the Michelle Munson-Serban Simu Keystone Research Scholar by Kansas State University, in 2017.

HAITHAM ABU-RUB (M'99–SM'07–F'18) received the M.Sc. degree in electrical engineering from the Gdynia Marine Academy, Gdynia, Poland, in 1990, and the Ph.D. degree from the Gdansk University of Technology, Gdansk, in 1995.

Since 2006, he has been with the Texas A&M University at Qatar, Doha, Qatar, where he is currently a Professor, the Chair of the Electrical and Computer Engineering Program, and the Managing Director of the Smart Grid Center Extension. He has authored more than 300 journal and conference papers and has earned and supervised many research projects. He is currently leading many projects on photovoltaic and hybrid renewable power generation systems with different types of converters and electric drives. He is the co-author of four books, two of which are published by Wiley. He is also an author or co-author of five book chapters. His research interests include energy conversion systems, including electric drives, power electronic converters, renewable energy, and smart grid.

Dr. Abu-Rub received many prestigious international awards, such as the American Fulbright Scholarship, the German Alexander von Humboldt Fellowship, the German DAAD Scholarship, and the British Royal Society Scholarship. He is also an Editor of several IEEE journals.